Title

# Lattice modeling of excavation damage in argillaceous clay formations: Influence of deformation and strength anisotropy



Authors
Kim, Kunhwi
Rutqvist, Jonny
Birkholzer, Jens

Publication Date
2020-04-01

DOI
10.1016/j.tust.2019.103196

Peer reviewed

# Lattice modeling of excavation damage in argillaceous clay formations: influence of deformation and strength anisotropy

Kunhwi Kim[a,*], Jonny Rutqvist[a], Jens Birkholzer[a]

[a]*Earth & Environmental Sciences Area, Lawrence Berkeley National Laboratory*
*1 Cyclotron Road, Berkeley, CA 94720, USA*

**Abstract**

This paper presents modeling of mechanical anisotropy in argillaceous rocks using an irregular lattice modeling approach, namely the rigid-body-spring network. To represent the mechanical anisotropy, new schemes are implemented in the modeling framework. The directionality of elastic deformation is resolved by modifying the element formulation with anisotropic elastic properties. The anisotropy of strength and failure characteristics is facilitated by adopting orientation-dependent failure criteria into the failure model. The verification of the improved modeling procedures is performed against theoretical model predictions for unconfined compression tests with various bedding orientations. Furthermore, excavation damage and fracturing processes in rock formations are simulated for different geomechanical configurations, such as rock anisotropy and tectonic heterogeneity. The simulated excavation damage characteristics are realistic and comparable with the actual field observation at a tunnel located in an argillaceous clay formation. The simulation results provide insights into the excavation damage zone

*Corresponding author.
*Email address:* `KunhwiKim@lbl.gov` (Kunhwi Kim)

*Preprint submitted to Tunnelling and Underground Space Technology* *October 20, 2019*

phenomena with an explicit representation of fracturing processes.
*Keywords:* Mechanical anisotropy, Argillaceous clay formation, Excavation damage zone, Fracture modeling, Rigid-body-spring network.

## 1. Introduction

The investigation of damage development around underground excavations is a key issue in a variety of geoengineering fields, including mining, tunneling, and nuclear waste disposal (Bäckblom and Martin, 1999; Tsang et al., 2005; Hudson et al., 2009). Similar stability problems of underground openings, such as well boreholes, are crucial in the reservoir engineering and drilling industry related to hydrocarbon extraction and geothermal energy exploitation (Zoback, 2007). Especially, in the field of deep geological disposal of nuclear waste, the excavation damage zone (EDZ) may have an adverse impact on the mechanical and hydrological properties of rock mass, thus affecting the isolation performance, and furthermore, the long-term safety of the repository (Levasseur et al., 2010).

Argillaceous clay formations are considered as potential host or cap rocks for deep geological disposal of nuclear waste due to their superior isolation and confinement characteristics. These characteristics include low permeability and diffusivity, high retention capacity for radionuclides, self-sealing features, and long-term stability of the geological environment (Marschall et al., 2006; Blümling et al., 2007). However, special geomechanical conditions in rock formations, such as low strength and mechanical anisotropy and unfavorable high degree of anisotropy of in-situ stresses at depth, increase vulnerability to excavation damage and fracture development around a tunnel or a shaft, which often brings about serious engineering difficulties during the construction and operation of deep underground repositories (Steiner, 1996; Martin et al., 1999; Bossart et al., 2004). Therefore, rational understanding of the geomechanical settings and the corresponding EDZ phenomena could help conducting more reliable performance and safety assessment of the deep clay-based repositories.

The mechanical behavior of argillaceous clay formations, such as shale, is greatly influenced by mechanical anisotropy, which is typically observed as a variation of elastic response, strength characteristics, and failure mechanisms with sample bedding orientation in laboratory experiments (McLamore and Gray, 1967; Niandou et al., 1997; Naumann et al., 2007). At a larger scale, this mechanical anisotropy directly affects the stability of underground structures and the observed failure behavior. Field observations from the Mont Terri underground research laboratory (URL) located in an indurated, over-consolidated clay shale, namely Opalinus Clay, indicate that the geometry and extent of the EDZ around tunnels are largely dependent on the relative orientation between bedding planes and the excavation axis (Marschall et al., 2006; Blümling et al., 2007; Labiouse and Vietor, 2014).

In this study, the mechanical anisotropy of argillaceous rocks is modeled within the rigid-body-spring network (RBSN) framework. A rock mass is rendered as a network of numerous spring sets connected with distinct one-dimensional elements (i.e., lattice elements), and the global mechanical behavior, including discrete fracturing process, is represented by the collection of local deformation and breakage of the spring sets. To represent the mechanical anisotropy within the modeling procedures, formulation of the element stiffness matrix is modified with anisotropic elastic configurations, and orientation-dependent failure criteria are introduced. Details of the proposed modeling schemes are presented in Section 2.

The improved modeling procedures are applied to simulate unconfined compression tests in Section 3, where variations of Young's modulus, uniaxial compressive strength, and fracture pattern with the bedding orientation are evaluated and verified against the theoretical model predictions. Furthermore, in Section 4, simulations of the EDZ evolutions are conducted for different geomechanical settings, and comparisons of the simulated EDZ features are made as a validation process.

## 2. Representation of mechanical anisotropy

The rigid-body-spring network (RBSN) approach has been used to investigate mechanics and fracture processes of geological systems, for which a rock mass is modeled as an assemblage of simple, two-node elements in a lattice structure. The irregular geometry of the lattice structure is defined by the dual Delaunay–Voronoi tesellation of a set of nodal points randomly generated in the domain (Okabe et al., 2000). This section presents methodologies for implementation of deformation and strength anisotropy in the lattice model.

### *2.1. Anisotropy of elastic deformability*

Figure 1 compares the formation of ordinary lattice elements and their modification for anisotropic elasticity. A 2D case is herein illustrated for plain description, but this scheme has been developed within the 3D modeling framework. A lattice element is formed from two neighboring nodes, $i$ and $j$, which are connected via rigid-body constraints to a zero-size spring set located at the center of the common Voronoi facet.

In the ordinary lattice model, the spring sets are oriented to their individual local $x$–$y$ coordinates defined by the Voronoi diagram (Fig. 1a). The spring coefficients are defined as (Kawai, 1978)

$$
\begin{aligned}
k_x &= \alpha_1 E \frac{A_{ij}}{h_{ij}} \\
k_y &= \alpha_2 k_x \\
k_\phi &= E \frac{I_\phi}{h_{ij}}
\end{aligned} \tag{1}
$$

where $A_{ij}$ is the area of the common Voronoi facet; $h_{ij}$ is the distance between the element nodes; and $I_\phi$ is the moment of inertia of the facet area. Factors $\alpha_1$ and $\alpha_2$ are adjusted to obtain global representation of Young's modulus $E$ and Poisson's ratio $\nu$. For the special case of $\alpha_1 = \alpha_2 = 1$, the lattice model provides an elastically homogeneous and isotropic representation of $E$, although the corresponding value of $\nu = 0$ (Bolander and Saito, 1998; Yip et al., 2005). In the new scheme for anisotropic representation, by comparison, the spring sets are aligned to the direction of bedding planes in $N-P$ coordinates (Fig. 1b). The stiffness coefficients in Eq. 1 can be modified for anisotropic elastic properties about the orthogonal $N-$ and $P-$axes:

$$
\begin{aligned}
k_N &= E_N \frac{A_{ij}}{h_{ij}} \\
k_P &= E_P \frac{A_{ij}}{h_{ij}} \\
k_\varphi &= E_N \frac{I_\phi}{h_{ij}}
\end{aligned} \tag{2}
$$

where $E_N$ and $E_P$ are Young's moduli normal and parallel to bedding, respectively, which can be directly adopted from laboratory measurements.

As seen in Fig. 1b, the kinematics of the nodes and elements can be represented in three distinct coordinate systems: global $X-Y$ coordinates based on domain construction; local $x-y$ coordinates for individual elements; and global $N-P$ coordinates related to the bedding orientation. The anisotropic material matrix

$\mathbf{D} = \mathrm{diag}[k_N,\ k_P,\ k_\varphi]$ for each lattice element is established in $N-P$ coordinates, then transformed to the spring set stiffness matrix in local $x-y$ coordinates using the coordinate transformation (McGuire and Gallagher, 1979):

$$\mathbf{k_s} = \mathbf{\Gamma}^{\mathrm{T}}\mathbf{D}\mathbf{\Gamma} \tag{3}$$

where $\mathbf{\Gamma}$ is the $3 \times 3$ coordinate transformation matrix from $x-y$ coordinates to $N-P$ coordinates:

$$\mathbf{\Gamma} = \begin{bmatrix} Nx & Ny & 0 \\ Px & Py & 0 \\ 0 & 0 & 1 \end{bmatrix} \tag{4}$$

The first $2{\times}2$ entries in $\gamma$ are the direction cosines between the bedding orientation and the local element axes.

The element stiffness matrix $\mathbf{k_e}$, relating the generalized local forces and element nodal displacements, is derived from $\mathbf{k_s}$ pre- and post-multiplied by the geometric matrix (Bolander and Saito, 1998; Berton and Bolander, 2006):

$$\mathbf{k_e} = \mathbf{B}^{\mathrm{T}}\mathbf{k_s}\mathbf{B} \tag{5}$$

The conversion of $\mathbf{k_e}$ to the global coordinates is obtained by another coordinate transformation:

$$\mathbf{K_e} = \mathbf{T}^{\mathrm{T}}\mathbf{k_e}\mathbf{T} \tag{6}$$

where $\mathbf{T}$ is the transformation matrix relating local $x-y$ and global $X-Y$ coordinate systems. The transformed element stiffness matrices, built for individual lattice elements, are assembled into the global stiffness matrix to solve the system equilibrium equations.

## 2.2. Anisotropy of strength

This study employs a Mohr–Coulomb model to determine brittle failure of lattice elements. The stress state of each lattice element is represented as a Mohr circle in the stress space, which is assessed by a limiting surface for possible failure conditions. Herein, a weak-plane failure model is used to provide anisotropic failure characteristics. This model assumes that the strength anisotropy is attributed to conditional failure on a particular orientation of a plane, where the material strength is significantly weaker. This model concept has a physical basis because the bedding planes in sedimentary rocks are generally recognized as planes of weakness (Pariseau, 2006; Fjær et al., 2008).

Figure 2 illustrates two distinct situations of orientation-dependent failure in the Mohr–Coulomb model. The material has two failure criteria—one intrinsic, isotropic criterion and one for the weak planes—and correspondingly two failure surfaces (Jaeger, 1960). The intrinsic failure criterion is given by the cohesive strength $c$, internal friction angle $\phi$, and tension cut-off $f_t$. Analogously, the weak-plane failure criterion is defined by lower values of the strength parameters $c_w$, $\phi_w$, and $f_{t,w}$. Consider the stress state in the rock specimen is such that the Mohr circle intersects the weak-plane failure surface at two points with angles $2\psi_1$ and $2\psi_2$ (Fig. 2a), and the material with a bedding orientation $\psi_1 < \beta < \psi_2$ will fail along the bedding planes at a lower stress level. However, if the bedding orientation $\beta$ is projected below the weak-plane failure surface, as shown in Fig. 2b, the material will fail across the bedding planes with the failure angle $\psi = 45° + \phi/2$ at a higher stress level.

For the confined stress configuration ($\sigma_1 > \sigma_2 = \sigma_3 > 0$), the two failure criteria limit the stress states, which can be theretically defined as follows (Jaeger et al., 2007):

$$\sigma_1 - \sigma_3 = 2\frac{c \cos\phi + \sigma_3 \sin\phi}{1 - \sin\phi} \tag{7}$$

for the intrinsic failure criterion; and

$$\sigma_1 - \sigma_3 = 2\frac{c_w \cos\phi_w + \sigma_3 \sin\phi_w}{\sin 2\beta \cos\phi_w - (1 + \cos 2\beta)\sin\phi_w} \tag{8}$$

for the weak-plane failure criterion. The criterion that predicts the lowest strength for a given orientation $\beta$ is always the relevant criterion in the failure model. In that sense, the anisotropic strength could vary with the bedding orientation of the sample.

## 3. Unconfined compression tests

The proposed modeling schemes are verified in the simulations of unconfined compression tests for transversely isotropic rock specimens. Consider a cylindrical core sample subjected to a uniaxial compression load, in which the bedding planes form an angle $\theta$ from the axial loading direction (see Fig. 3a). We have conducted simulations for eight cases of angles to bedding: $\theta = -15°$; $0°$ (parallel to loading axis); $15°$; $30°$; $45°$; $60°$, $75°$; and $90°$ (normal to loading axis). As shown in Fig. 3b, a core sample with a diameter of 50 mm and a height of 100 mm is discretized with 15,047 nodes and 76,730 elements. Extra layers of nodes and elements are padded at the top and bottom of the cylinder to provide uniform axial strain along the section, where a displacement controlled boundary condition is applied to deform the sample up to 0.3 mm in compression. The anisotropic properties of the core material are adopted from the experimental results for the Opalinus Clay samples (Bossart, 2011), which are listed in Table 1.

The resulting stress-strain curves for the eight cases of bedding orientations are plotted in Fig. 4. The stress response is calculated by averaging the sum of reaction forces monitored at the padding layers over the cross sectional area of the sample. The height of the core sample is taken as the gauge length to derive global axial strain from the boundary displacements. The stress linearly increases with the strain to the peak stress and sharply decreases over the peak, involving brittle failure. The linear slope and the peak of the response curve vary with the bedding orientation, which reflects the mechanical anisotropy of the rock material. Note that the response curves for $\theta = -15°$ and $15°$ coincide closely with each other because of the symmetric bedding orientations with the same angle from the loading axis.

The linear slope of each stress-strain curve is taken as the global Young's modulus of the sample and compared with a theory in Fig. 5. The Young's modulus of a transversely isotropic material with an angle $\theta$ from the loading axis to the bedding is theoretically obtained by Pariseau (2006):

$$\frac{1}{E} = \frac{\cos^4\theta}{E_P} + \left(\frac{1}{G_a} - \frac{2\nu_a}{E_P}\right)\sin^2\theta\cos^2\theta + \frac{\sin^4\theta}{E_N} \tag{9}$$

where $G_a$ and $\nu_a$ are the relevant shear modulus and Poisson's ratio for the anisotropic case, respectively. With an approximation of $G_a = 1/\left(\frac{1}{E_P} + \frac{1}{E_N}\right)$ for zero Poisson's ratio, Eq. 9 can be rewritten as

$$\frac{1}{E} = \frac{\cos^2\theta}{E_P} + \frac{\sin^2\theta}{E_N} \tag{10}$$

The variation of Young's modulus from the simulations shows a good agreement with the theoretical model prediction.

The peak stress captured from the stress-strain response can be regarded as the uniaxial compressive strength. Figure 6 shows the simulated uniaxial compressive strengths for the cases of different angles to bedding. The orientation-dependent failure criteria presented in Section 2.2 limit the critical stress state of the anisotropic material. By imposing the lateral unconfined condition ($\sigma_3 = 0$) and substituting the relevant strength parameters into Eqs. 7 and 8, the theoretical uniaxial compressive strength at an angle to bedding $\theta = 90° - \beta$ can be determined as the lowest strength between

$$UCS = \frac{2c_P \cos\phi_P}{1 - \sin\phi_P} \tag{11}$$

and

$$UCS = \frac{2c_N \cos\phi_N}{\sin 2\theta \cos\phi_N - (1 - \cos 2\theta) \sin\phi_N} \tag{12}$$

This theoretical model prediction is also plotted as a function of the angle to bedding $\theta$ in Fig. 6, which is perfectly in line with the simulated uniaxial compressive strengths. However, the material exhibits anisotropic strengths only when the bedding orientations fall in a certain range for the weak-plane failure and otherwise a constant strength involved with the intrinsic isotropic failure, which is attributed to the discontinuous set of a single plane of weakness in the failure model. More sophisticated models such that weak planes and the corresponding strength param-eters vary continuously with the bedding orientation could provide more realistic representation of rock anisotropy (McLamore and Gray, 1967; Hoek and Brown, 1980; Pietruszczak and Mroz, 2001).

Figure 7 presents fracture patterns within the samples at the final loading stage (0.003 of axial strain). Overall, cracks tend to propagate in the direction of bedding planes, especially for the cases of low inclination angles of bedding planes from the loading axis. In these cases, weak-plane failure along the bedding planes is selected as the relevant mechanism to proceed the material failure. A comparison of Figs. 7a and c indicates that symmetric bedding orientations about the loading axis naturally lead to symmetric patterns of fracture development. In the exceptional case with 45° to bedding (Fig. 7e), the fractures align perpendicular to the bedding planes, which form a thick shear band across the sample.

In the simulations of unconfined compression tests, the elastic deformability and failure characteristics of the anisotropic rock material are rationally demonstrated. Various bedding orientations of the core samples are represented without the need of orientation-dependent mesh geometry, but rather with inherent anisotropy of lattice elements. Also, the mechanical parameters are uniformly assigned to the elements irrespective of their local orientations, which contrasts to other modeling approaches using heterogeneous parameters dependent on the direction of element (Lisjak et al., 2014, 2015). In the next section, the modeling procedures are further validated through simulations of excavation damage and fracturing processes in rock formations.

## 4. Excavation damage and fracture development in argillaceous clay formations

### *4.1. HG-A microtunnel at the Mont Terri site*

The evolution of excavation damage zone (EDZ) near a tunnel is simulated and validated against the field observation at the HG-A test site. A circular microtunnel with the length of 13 m and the diameter of 1.04 m is located at the Mont Terri URL near Saint-Ursanne, Switzerland. The host rock, Opalinus Clay, is relatively homogeneous in meter-scale, but pronounced anisotropy with bedding planes is discovered at millimeter-scale (Yong et al., 2010). The rock formation surrounding the HG-A tunnel is highly fractured with a sub-meter spatial frequency although the fracture permeability is not significant, which indicates that fractures are mostly closed under natural stress conditions (Marschall et al., 2006, 2008).

One main purpose of the HG-A test is to provide data on the geomechanical and hydrogeological effects due to the presence of the EDZ around the tunnel. Although the long-term physical features observed in the test are related to coupled hydro-mechanical processes, herein the problem is simplified by assuming a constant uniform pore pressure such that the excavation damage and fracturing processes can be reckoned as short-term mechanical-only responses. This assumption is valid up until an early tunneling stage, where mechanical deformations occur much more quickly than water flow and hydrological processes in the rock formation, and the mechanical equilibrium is held within a rapid (undrained) excavation (Liu et al., 2013). In the actual excavation of the HG-A tunnel, the drilling progress was rather quick and smooth (Marschall et al., 2006), so pure mechanical simulations are applicable to this case, where relevant EDZ phenomena could be captured.

Figure 8 shows excavation damage around the microtunnel. Anisotropic properties of the rock material and heterogeneity of tectonic fault formations, as well as anisotropic in-situ stress conditions, result in non-uniform damage around the tunnel. Major buckling and spalling phenomena between 10 and 11 o'clock and less distinct buckling at about 5 o'clock are observed along the tunnel wall, which indicates that the tunnel is running parallel to the strike of inclined bedding planes (Marschall et al., 2006). On the other hand, wedge-shaped damage structures with extension joints mapped on the side surfaces (3 to 4 o'clock and 9 to 10 o'clock) are identified as stress-induced breakouts.

In this study, we investigate the effects of rock anisotropy and tectonic heterogeneity on the EDZ phenomena. Figure 9 presents three simulations cases with different geomechanical settings: (I) in-plane isotropy and intact formation; (II) in-plane anisotropy and intact formation; and (III) in-plane anisotropy and fault formation. Anisotropic in-situ stresses of $\sigma_v$ = 6.5 MPa in the vertical direction and $\sigma_h$ = 4.5 MPa in the horizontal direction are adopted as a confinement condition (Martin and Lanyon, 2003), and a uniform pore pressure of 1.5 MPa is applied in the modeling domain. For Cases II and III, the bedding planes are oriented at 45° from the horizontal axis (Figs. 9b and c), and additionally for Case III three discrete fault planes are placed around the tunnel (Fig. 9c).

Figure 10 depicts the Voronoi discretizations of a 10 m square domain for the excavation damage simulations. Predicted EDZ area around the tunnel is finely meshed, and the nodal density is graded towards the domain boundaries for computational efficiency. The circular tunnel with 1.04 m diameter is initially filled with the Voronoi cells and lattice elements. The excavation process is realized by gradually reducing the spring stiffnesses, internal element forces, and pore pressure of the elements to void the tunnel domain, for which an exponential decay is assumed to set the reduction of the values to $10^{-6}$ of the original values at the end of 100 loading steps. Herein, gravity loads are ignored throughout the simula-tions because the gravity forces may have a minor influence compared to the effect of in-situ stresses in case of relatively deep, small excavations (Carranza-Torres and Fairhurst, 1997). As shown Fig. 10b, fault planes are explicitly represented in the mesh, and low strength parameters are assigned to the corresponding el-ements: tensile strength $f_{t,f}$ = 0.5 MPa; cohesion $c_f$ = 1.0 MPa; and friction angle $\phi_f$ = 23°. Rock properties are set as listed in Table. 1. Note that while clay shale may exhibit plastic deformations or residual stress responses under confined stress conditions (Parisio et al., 2015), this study simply assumes the rock material around the tunnel opening undergoes brittle failure with unconfined conditions.

### 4.2. Discussion on simulation results

From the simulations of the EDZ evolutions, the resulting damage patterns and the contours of the magnitudes of the major principal stress and the minor principal stress are given in Figures 11 to 13. For Case I with isotropic rock properties, excavation-induced cracks stretch out in the direction perpendicular to the major confining stress to result in the formation extensive breakouts or v-shaped notches (see Fig. 11a), which is a failure pattern frequently found under anisotropic in-situ stress conditions (Martin et al., 1999; Read, 2004; Perras and Diederichs, 2016). As seen in Figs. 11b and c, the in-situ stress field is altered by the excavation. The failed zones exhibit low magnitudes of stresses due to softening and weakening effects of the fractures, however, the redistribution of stresses is highly concentrated close to the notch tips. In the outer region, the disturbed stress field displays quite symmetric contours about the vertical and horizontal axes crossing at the center of the tunnel.

The simulation results for Case II, presented in Fig. 12, show failure characteristics influenced by the anisotropy of deformability and strength. As shown in Fig. 12a, more pronounced cracks and breakouts at the tunnel wall are concentrated and oriented along the direction normal to the bedding planes. Compared to the stress contours in the previous case, the contour patterns are asymmetric and inclined towards the bedding orientation (see Figs. 12b and c), which may be attributed to the anisotropic rock properties and the inclined failed zones.

For Case III with anisotropic rock properties and fault planes, the EDZ evolution involves more complex failure processes. Distinct shear failures occur along the fault planes in the early stage of excavation, and then rock cracking grows from the fault planes. The failed zones illustrated in Fig. 13a conform to the estimation of damaged zones from the field observation (see Fig. 8). One notable feature in the fractured damage pattern is that the crack growth in the rock is somewhat controlled by the fault planes, so that the cracks do not propagate across the faults. Figures 13b and c show the stress field perturbed by the fault planes, where discontinuous stress contours are spotted in the fractured zones and extended along the fault planes.

## 5. Conclusions

The evolution of excavation damage zone (EDZ) and the failure features around the tunnel excavation are found to be strongly related to the lithological properties of the rock formations, i.e., rock anisotropy due to the bedding planes. In this study, the rigid-body-spring network (RBSN) approach is used to simulate the mechanically anisotropic behavior of argillaceous rocks. Since the original RBSN models generally provide the descriptions of isotropic systems, the modeling procedures have been modified and improved with new modeling schemes to represent the mechanical anisotropy. The spring coefficients of individual lattice elements are systematically formulated based on the bedding orientation, and in addition, a simple weak-plane failure model is adopted into the Mohr–Coulomb criteria to determine the local failure along the bedding planes. The improved modeling procedures can readily represent the anisotropic elasticity and effectively capture the orientation-dependent failure features and strength anisotropy.

Using the new schemes in the RBSN model, unconfined compression tests are simulated for transversely isotropic rock specimens, and the simulation results are verified against analytical solutions. Various bedding orientations of the samples can be reflected on the identical mesh without modifying or re-constructing the mesh geometry. From the stress-strain responses for the simulated cases, the global Young's moduli and the uniaxial compressive strengths are evaluated, which fall in line with the analytically determined values of anisotropic properties. Moreover, anisotropic failure characteristics are observed from the orientation of fracture development relative to the direction of bedding planes.

Next, the modeling procedures are applied to simulate the tunnel excavation in rock formations, where three cases of geomechanical settings are considered to make a comparative study on the EDZ phenomena. Several observations can be highlighted:

- The EDZ evolution in the isotropic rock formation is largely influenced by the in-situ stress field. Major failure and extensive breakouts are generated to build v-shaped notches from the tunnel wall in the direction perpendicular to the major principal compressive stress.

- In the presence of rock anisotropy, excavation-induced fractures are inclined to develop on the tunnel walls tangential to the bedding planes. Due to the anisotropic elastic properties, stress contours around the tunnel are asymmetric about the principal axis of in-situ stress and inclined to the bedding orientation.

- Tectonic faults can contribute to the heterogeneous excavation damage, where distinct shear failures occur along the fault planes and the stress contours are divided into discontinuous regions. The resulting fracture pattern in the damaged zones is also affected by the fault planes.

In summary, the simulations presented in this paper confirm the validity of the RBSN approach to model the EDZ evolutions in argillaceous rocks. The EDZ phenomena reproduced in the simulations are realistic and comparable with the actual EDZ observation at the HG-A microtunnel. The simulation results provide insights into the characterizations of excavation damage with an explicit representation of fracturing processes.

## Acknowledgment

This research is supported by the Spent Fuel and Waste Disposition Campaign, Office of Nuclear Energy of the U.S. Department of Energy, under Contract Number DE-AC02- 05CH11231 with Lawrence Berkeley National Laboratory.

## References

Bäckblom, G., Martin, C. D., 1999. Recent experiments in hard rocks to study the excavation response: Implications for the performance of a nuclear waste geological repository. Tunnelling and Underground Space Technology 14 (3), 377–394.

Berton, S., Bolander, J. E., 2006. Crack band model of fracture in irregular lattices. Computer Methods in Applied Mechanics and Engineering 195 (52), 7172–7181.

Blümling, P., Bernier, F., Lebon, P., Martin, C. D., 2007. The excavation damaged zone in clay formations time-dependent behaviour and influence on performance assessment. Physics and Chemistry of the Earth, Parts A/B/C 32 (8), 588–599.

Bolander, J. E., Saito, S., 1998. Fracture analyses using spring networks with random geometry. Engineering Fracture Mechanics 61 (5-6), 569–591.

Bossart, P., 2011. Characteristics of the Opalinus Clay at Mont Terri. Mont Terri Project, Wabern, Switzerland.

Bossart, P., Trick, T., Meier, P. M., Mayor, J.-C., 2004. Structural and hydrogeological characterisation of the excavation-disturbed zone in the Opalinus Clay (Mont Terri Project, Switzerland). Applied Clay Science 26, 429–448.

Carranza-Torres, C., Fairhurst, C., 1997. On the stability of tunnels under gravity loading, with post-peak softening of the ground. International Journal of Rock Mechanics and Mining Sciences 34 (3–4), 75.e1–75.e18.

Fjær, E., Holt, R. M., Horsrud, P., Raaen, A. M., Risnes, R. (Eds.), 2008. Petroleum Related Rock Mechanics, 2nd Edition. Vol. 53 of Developments in Petroleum Science. Elsevier.

Hoek, E., Brown, E. T., 1980. Empirical strength criterion for rock masses. Journal of Geotechnical and Geoenvironmental Engineering 106, 1013–1035.

Hudson, J. A., Bäckström, A., Rutqvist, J., Jing, L., Backers, T., Chijimatsu, M., Christiansson, R., Feng, X.-T., Kobayashi, A., Koyama, T., Lee, H.-S., Neretnieks, I., Pan, P.-Z., Rinne, M., Shen, B.-T., 2009. Characterising and modelling the excavation damaged zone in crystalline rock in the context of radioactive waste disposal. Environmental Geology 57 (6), 1275–1297.

Jaeger, J. C., 1960. Shear failure of anistropic rocks. Geological Magazine 97 (1), 65–72.

Jaeger, J. C., Cook, N. G. W., Zimmerman, R., 2007. Fundamentals of Rock Mechanics, 4th Edition. Wiley-Blackwell.

Kawai, T., 1978. New discrete models and their application to seismic response analysis of structures. Nuclear Engineering and Design 48, 207–229.

Labiouse, V., Vietor, T., 2014. Laboratory and in situ simulation tests of the excavation damaged zone around galleries in Opalinus Clay. Rock Mechanics and Rock Engineering 47 (1), 57–70.

Levasseur, S., Charlier, R., Frieg, B., Collin, F., 2010. Hydro-mechanical modelling of the excavation damaged zone around an underground excavation at Mont Terri Rock Laboratory. International Journal of Rock Mechanics and Mining Sciences 47 (3), 414–425.

Lisjak, A., Garitte, B., Grasselli, G., Müller, H., Vietor, T., 2015. The excavation of a circular tunnel in a bedded argillaceous rock (Opalinus Clay): Short-term rock mass response and FDEM numerical analysis. Tunnelling and Underground Space Technology 45, 227–248.

Lisjak, A., Grasselli, G., Vietor, T., 2014. Continuum–discontinuum analysis of failure mechanisms around unsupported circular excavations in anisotropic clay shales. International Journal of Rock Mechanics and Mining Sciences 65, 96–115.

Liu, H. H., Houseworth, J., Rutqvist, J., Zheng, L., Asahina, D., Li, L., Vilarrasa, V., Chen, F., Nakagawa, S., Finsterle, S., Doughty, C., Kneafsey, T., Birkholzer, J., 2013. Report on thmc modeling of the near field evolution of a generic clay repository: Model validation and demonstration. Tech. Rep. FCRD-UFD-2013-000244, Lawrence Berkeley National Laboratory, Berkeley, CA.

Marschall, P., Distinguin, M., Shao, H., Bossart, P., Enachescu, C., Trick, T., 2006. Creation and evolution of damage zones around a microtunnel in a claystone formation of the Swiss Jura Mountains. In: SPE International Symposium and Exhibition on Formation Damage Control. No. SPE-98537-PP. Society of Petroleum Engineers.

Marschall, P., Trick, T., Lanyon, G. W., Delay, J., Shao, H., 2008. Hydromechanical evolution of damaged zones around a microtunnel in a claystone formation of the Swiss Jura Mountains. In: The 42nd US Rock Mechanics Symposium (USRMS). No. ARMA-08-193. American Rock Mechanics Association.

Martin, C. D., Kaiser, P. K., McCreath, D. R., 1999. Hoek-Brown parameters for predicting the depth of brittle failure around tunnels. Canadian Geotechnical Journal 36 (1), 136–151.

Martin, C. D., Lanyon, G. W., 2003. Measurement of in-situ stress in weak rocks at Mont Terri Rock Laboratory, Switzerland. International Journal of Rock Mechanics and Mining Sciences 40 (7), 1077–1088.

McGuire, W., Gallagher, R. H., 1979. Matrix Structural Analysis. John Wiley & Sons, New York.

McLamore, R., Gray, K. E., 1967. The mechanical behavior of anisotropic sedimentary rocks. Journal of Engineering for Industry 89 (1), 62–73.

Naumann, M., Hunsche, U., Schulze, O., 2007. Experimental investigations on anisotropy in dilatancy, failure and creep of Opalinus Clay. Physics and Chemistry of the Earth, Parts A/B/C 32 (8), 889–895.

Niandou, H., Shao, J. F., Henry, J. P., Fourmaintraux, D., 1997. Laboratory investigation of the mechanical behaviour of Tournemire shale. International Journal of Rock Mechanics and Mining Sciences 34 (1), 3–16.

Okabe, A., Boots, B., Sugihara, K., Chiu, S. N., 2000. Spatial Tessellations: Concepts and Applications of Voronoi Diagrams. John Wiley & Sons.

Pariseau, W. G., 2006. Design Analysis in Rock Mechanics. CRC Press, London, UK.

Parisio, F., Samat, S., Laloui, L., 2015. Constitutive analysis of shale: a coupled damage plasticity approach. International Journal of Solids and Structures 75-76, 88–98.

Perras, M. A., Diederichs, M. S., 2016. Predicting excavation damage zone depths in brittle rocks. Journal of Rock Mechanics and Geotechnical Engineering 8 (1), 60–74.

Pietruszczak, S., Mroz, Z., 2001. On failure criteria for anisotropic cohesive-frictional materials. International Journal for Numerical and Analytical Methods in Geomechanics 25 (5), 509–524.

Read, R. S., 2004. 20 years of excavation response studies at AECL's Underground Research Laboratory. International Journal of Rock Mechanics and Mining Sciences 41 (8), 1251–1275.

Steiner, W., 1996. Tunnelling in squeezing rocks: Case histories. Rock Mechanics and Rock Engineering 29 (4), 211–246.

Tsang, C.-F., Bernier, F., Davies, C., 2005. Geohydromechanical processes in the Excavation Damaged Zone in crystalline rock, rock salt, and indurated and plastic clays—in the context of radioactive waste disposal. International Journal of Rock Mechanics and Mining Sciences 42 (1), 109–125.

Yip, M., Mohle, J., Bolander, J. E., 2005. Automated modeling of three-dimensional structural components using irregular lattices. Computer-Aided Civil and Infrastructure Engineering 20 (6), 393–407.

Yong, S., Kaiser, P. K., Loew, S., 2010. Influence of tectonic shears on tunnel-induced fracturing. International Journal of Rock Mechanics and Mining Sciences 47 (6), 894–907.

Zoback, M. D., 2007. Reservoir Geomechanics. Cambridge University Press.

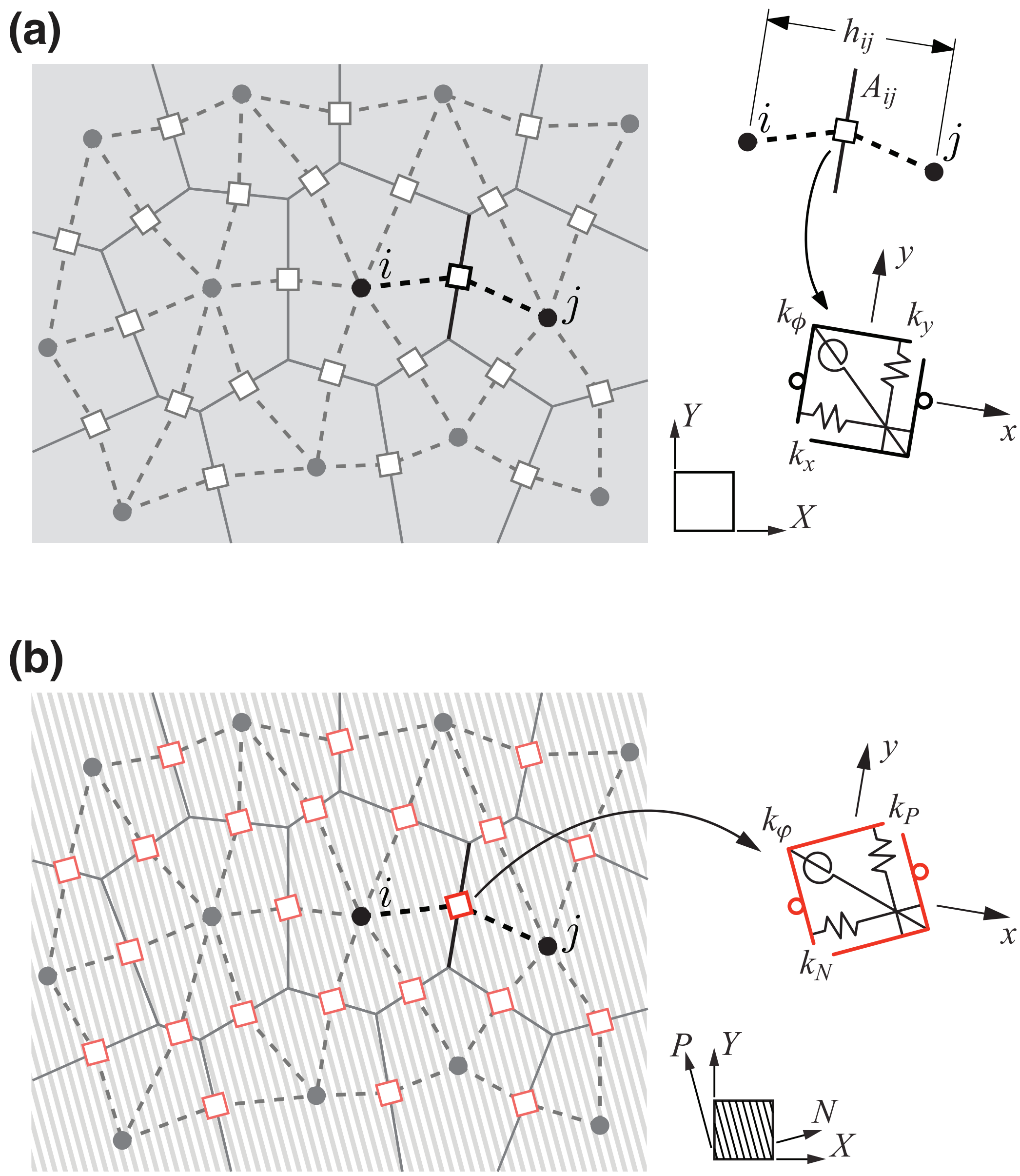


Figure 1: Modification of rigid-body-spring elements in an identical lattice structure: (a) original spring sets based on the direction of Voronoi facets (local $x$−$y$ coordinate systems); and (b) spring sets aligned to the global bedding orientation ($N$−$P$ coordinate system).

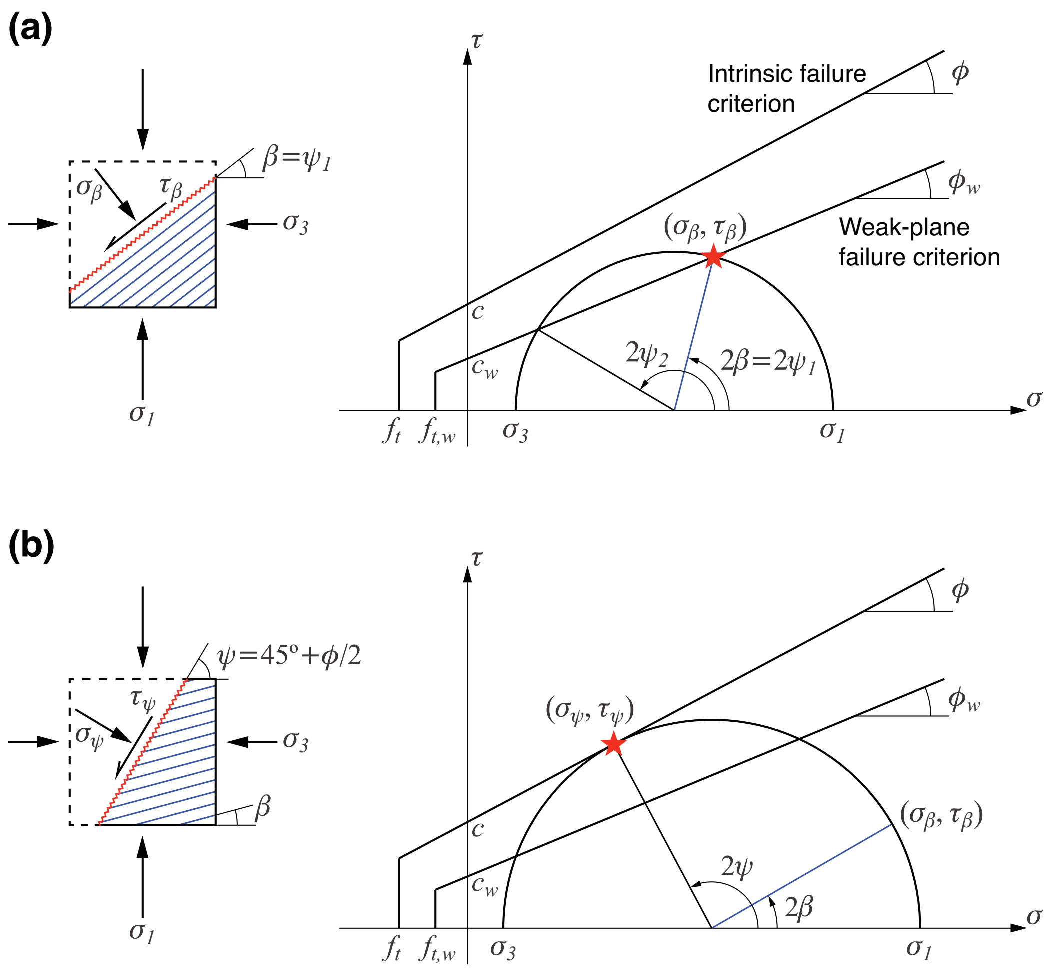


Figure 2: Orientation-dependent failure criteria in Mohr–Coulomb model: (a) weak-plane failure along the bedding; and (b) intrinsic failure across the bedding.

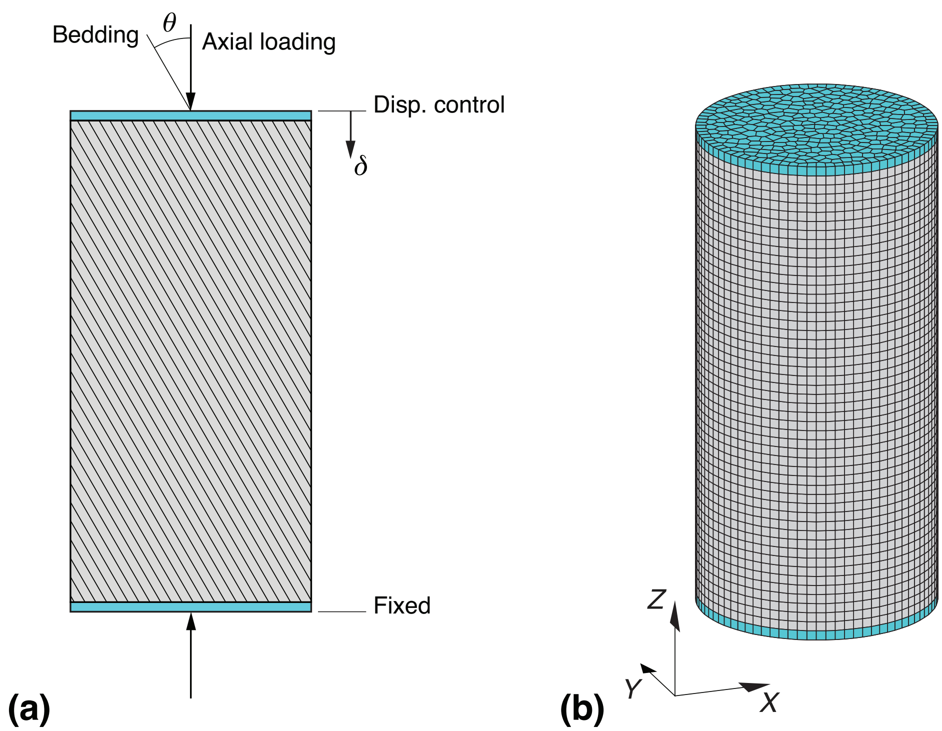


Figure 3: Uniaxial compression tests: (a) schematic drawing of the test program; and (b) 3D Voronoi discretization of a specimen model.

Table 1: Anisotropic mechanical properties of Opalinus Clay (Bossart, 2011)

| Rock properties | Parallel to bedding | Normal to bedding |
|---|---|---|
| Young's modulus | $E_P$ = 15.5 GPa | $E_N$ = 9.5 GPa |
| Uniaxial tensile strength | $f_{t,P}$ = 2.0 MPa | $f_{t,N}$ = 1.0 MPa |
| Cohesion† | $c_P$ = 5.5 MPa | $c_N$ = 2.2 MPa |
| Internal friction angle | $\phi_P = 25°$ | $\phi_N = 25°$ |

† Bossart (2011) suggested three different values for cohesion or shear strength: maximum value of 5.5 MPa (parallel to bedding); minimum value of 2.2 MPa (normal to bedding); and the third value of 1 MPa (shear strength of bedding planes). In this study, 2.2 MPa is taken as a cohesive strength normal to bedding, as stated.

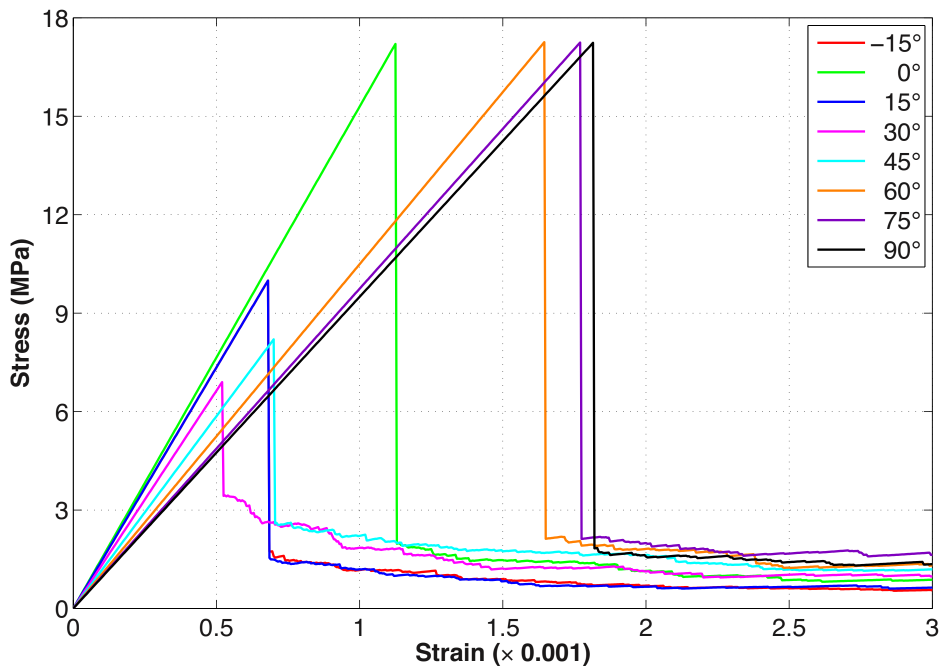


Figure 4: Stress-strain responses for various angles to bedding.

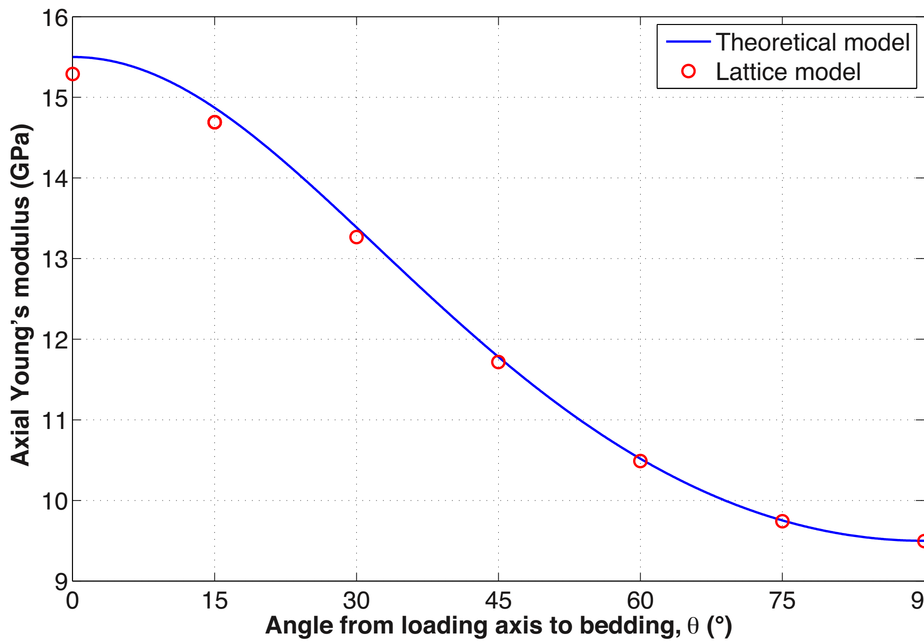


Figure 5: Comparison of simulated Young's modulus with the theoretical model prediction (Eq. 10) for different bedding orientations.

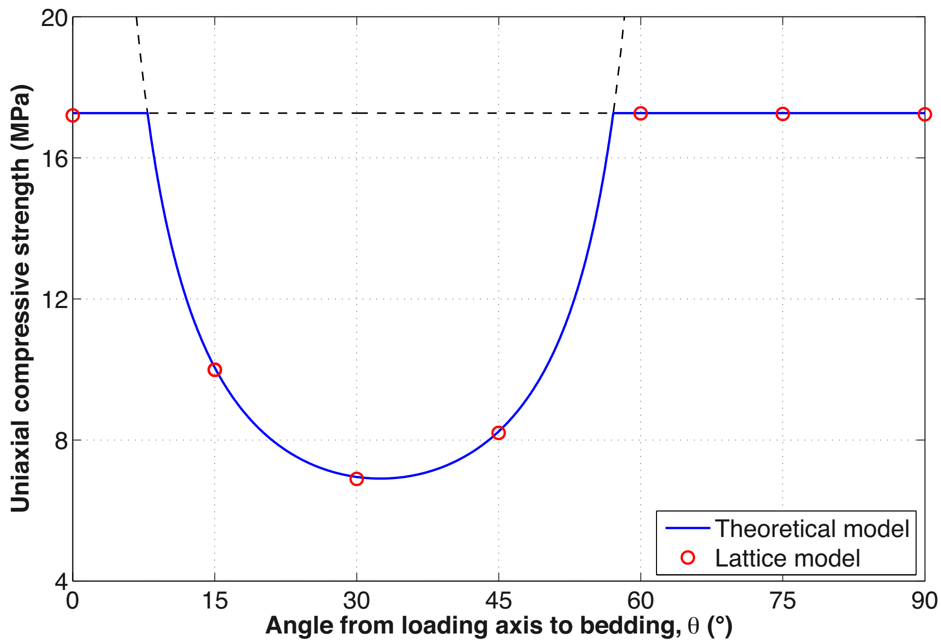


Figure 6: Comparison of simulated uniaxial compressive strength with the theoretical model prediction (determined by Eqs. 11 and 12) for different bedding orientations.

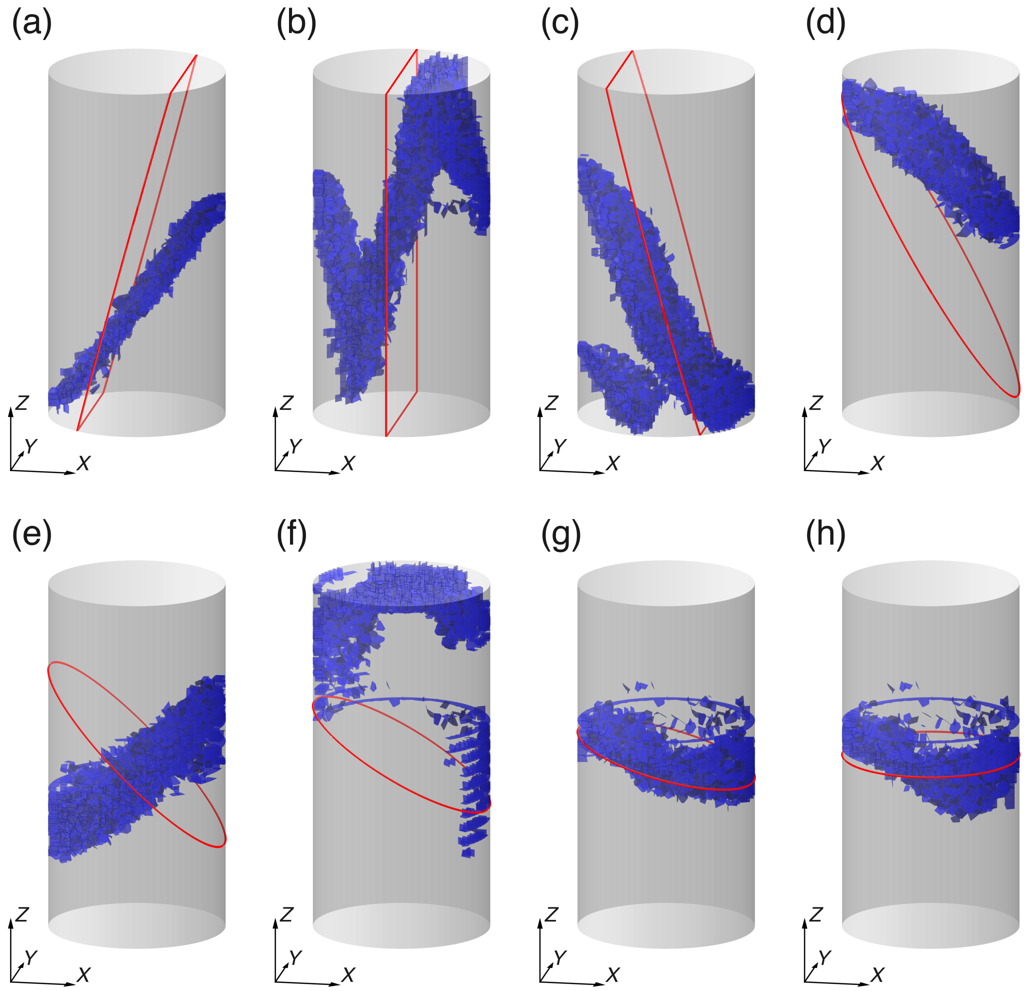


Figure 7: Comparison of fracture patterns for angles to bedding, $\theta$ = (a) $-15°$; (b) $0°$; (c) $15°$; (d) $30°$; (e) $45°$; (f) $60°$; (g) $75°$; and (h) $90°$. Note that the red contour of cylindric section for each case refers to the representative bedding plane.

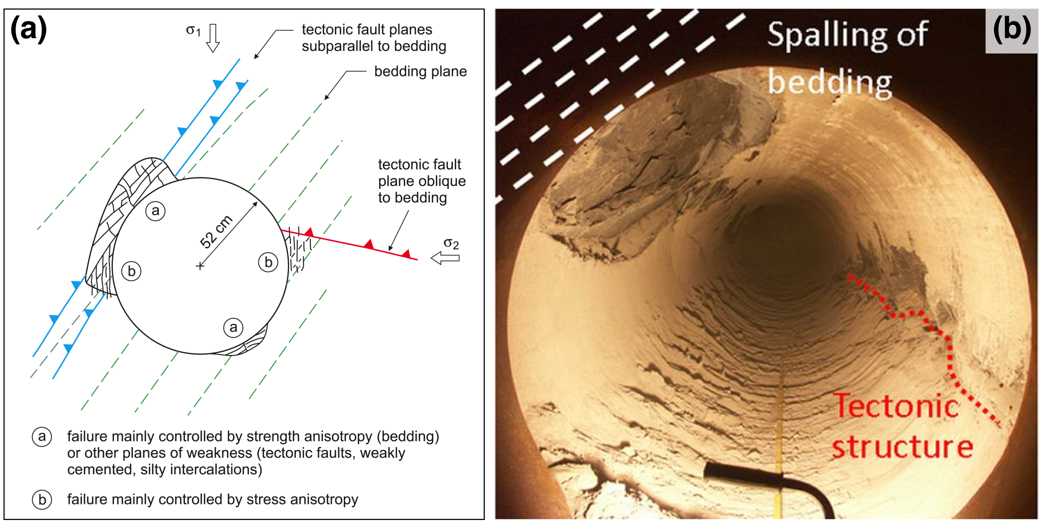


Figure 8: Excavation damage of the HG-A microtunnel: (a) conceptual diagram of the damaged zones and fault traces around the tunnel; and (b) observed damage formation along the tunnel (adapted from Marschall et al. 2006).

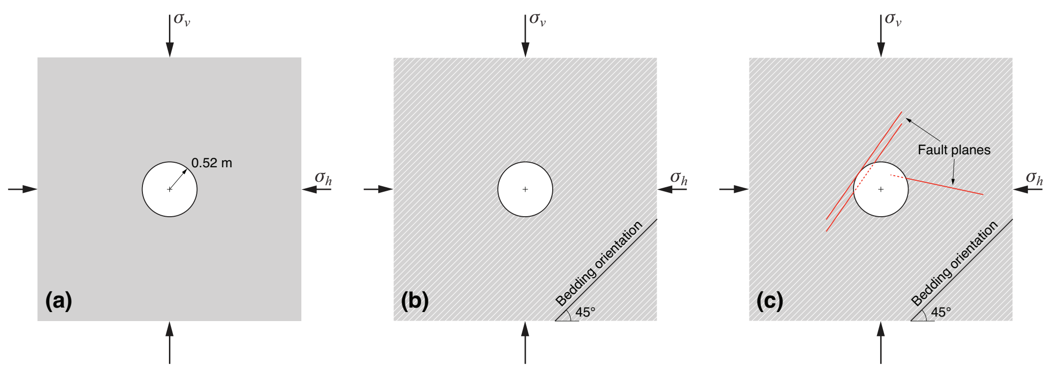


Figure 9: Modeling cases for three different geomechanical settings: (a) Case I for in-plane isotropy and intact formation; (b) Case II for in-plane anisotropy and intact formation; and (c) Case III for in-plane anisotropy and fault formation.

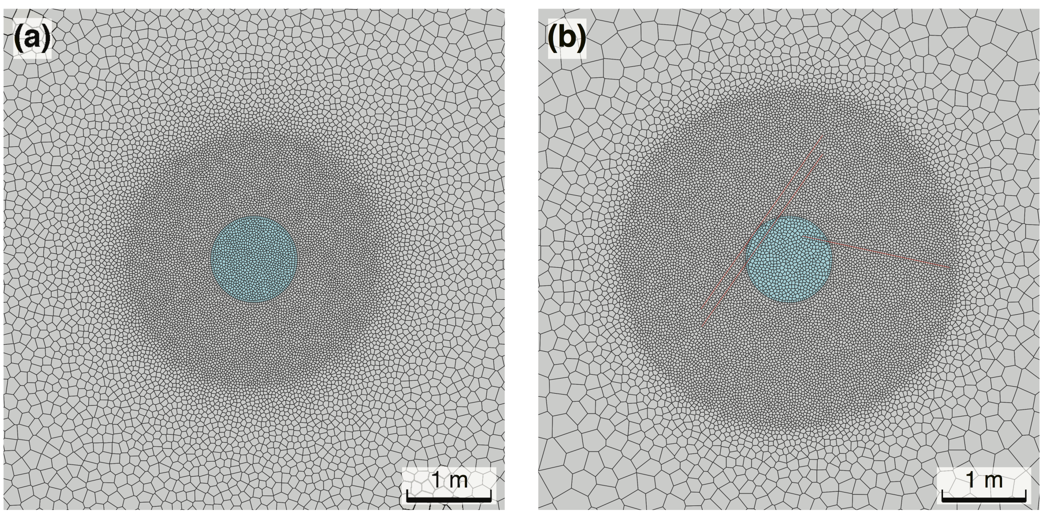


Figure 10: Voronoi discretizations for modeling tunnel geometries in (a) intact formation (Cases I and II) and (b) fault formation (Case III).

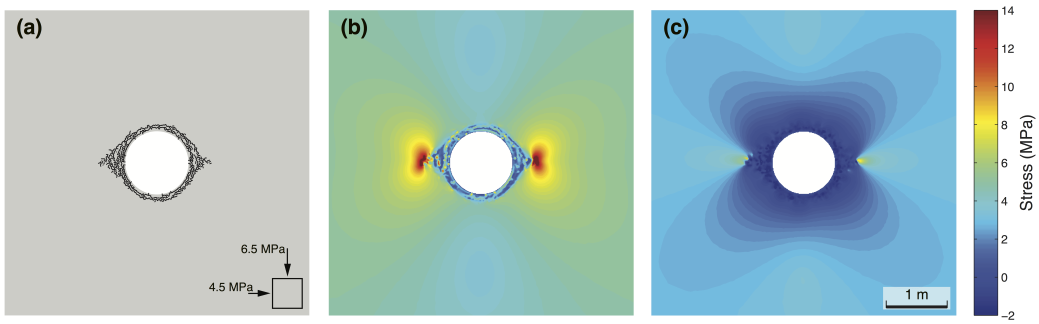


Figure 11: Results at the final stage of the simulation for Case I with in-plane isotropy and intact formation: (a) fracture pattern; (b) major principal stress; and (c) minor principal stress.

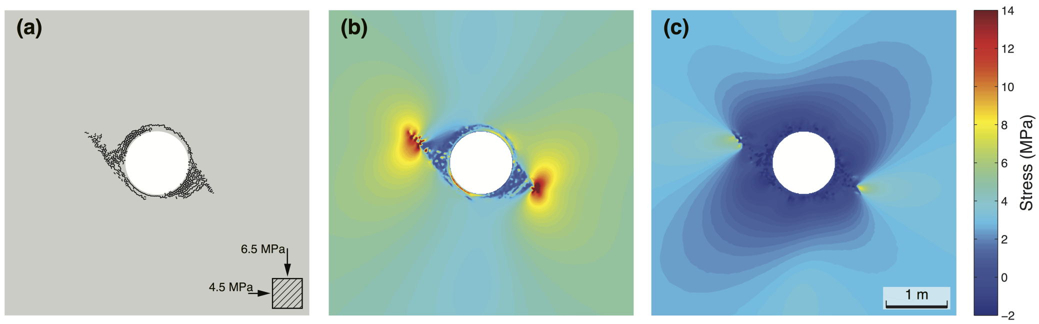


Figure 12: Results at the final stage of the simulation for Case II with in-plane anisotropy and intact formation: (a) fracture pattern; (b) major principal stress; and (c) minor principal stress.

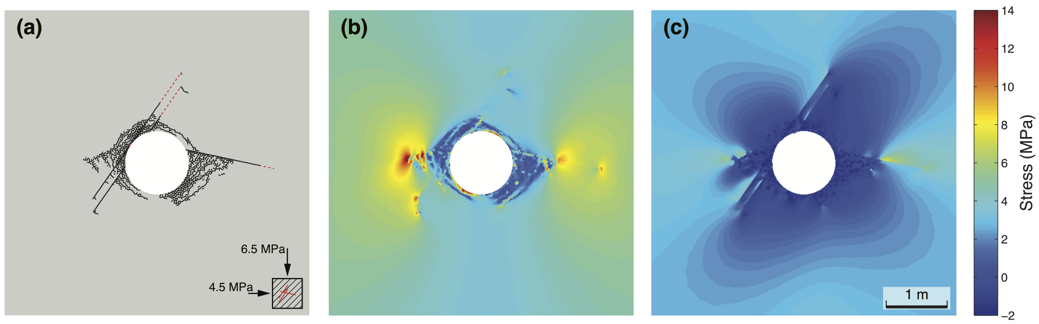


Figure 13: Results at the final stage of the simulation for Case III with in-plane anisotropy and fault formation: (a) fracture pattern; (b) major principal stress; and (c) minor principal stress.